Analog field-scale acoustic study of volcanic eruption directivity using a tiltable liquid-nitrogen charged water cannon

Author #1: Arthur D. Jolly, 1) U.S Geological Survey, Hawaiian Volcano Observatory Suite A8, 1266 Kamehameha Avenue, Hilo, HI, 96720 USA, ajolly@usgs.gov; 2) GNS Science, 1 Fairway Drive, Avalon, Lower Hutt 5010, New Zealand

Author #2: Ben Kennedy, University of Canterbury, Department of Geological Sciences, Christchurch, New Zealand institutional address, ben.kennedy@canterbury.ac.nz

Author #3: Robin S. Matoza, Department of Earth Science and Earth Research Institute, University of California, Santa Barbara, CA, USA, rmatoza@ucsb.edu

Author #4: Alexandra M. Iezzi, Department of Earth Science and Earth Research Institute, University of California, Santa Barbara, CA, USA, amiezzi@ucsb.edu

Author #5: Bruce Christenson, [5]GNS Science, Avalon, New Zealand, b.christenson@gns.cri.nz

Author #6: Richard Johnson, Wairakei Research Centre, 114 Karetoto Rd., Wairakei, New Zealand, r.johnson@gns.cri.nz

Author #7: Amilea Sork, University of Canterbury, Department of Geological Sciences, Christchurch, New Zealand, ars115@uclive.ac.nz

Author #8: David Fee, Alaska Volcano Observatory, Geophysical Institute, University of Alaska-Fairbanks, USA, dfee1@alaska.edu

Indicate the corresponding author: Arthur D. Jolly

Abstract

Laterally directed explosive eruptions are responsible for multiple fatalities over the past decade and are an increasingly important volcanology problem. To understand the

energy dynamics for these events, we collected field-scale explosion data from nine acoustic sensors surrounding a tiltable cannon as part of an exploratory experimental design. For each cannon discharge, the blast direction was varied systematically at 0°, 12°, and 24° from vertical, capturing acoustic wavefield directivity related to the tilt angle. While each event was similar in energy discharge potential, the resulting acoustic signal features were variable event-to-event, producing non-repetitious waveforms and spectra. Systematic features were observed in a subset of individual events for vertical and lateral discharges. For vertical discharges, the acoustic energy had a uniform radiation pattern. The lateral discharges showed an asymmetric radiation pattern with higher frequencies in the direction of the blast and depletion of those frequencies behind the cannon. Results suggest that, in natural volcanic systems, near-field blast directionality may be elucidated from acoustic sensors in absence of visual data, with implications for volcano monitoring and hazard assessment.

Keywords

volcanic eruptions, lateral-blast, source dynamics, source processes, volcano acoustics, directivity, directionality, Doppler-shift, waveform template clustering, source evolution

1. Introduction

Small-scale volcanic eruptions from phreatic to Strombolian systems are especially important from a hazard and impact perspective. While such systems produce very small eruptions and small hazard footprints and magnitudes, they pose out-sized risks due to the exposure of sightseers to these frequent events (Erfurt-Cooper, 2014; Fitzgerald et al., 2017). Visitors are often attracted to these beautiful landscapes, unusual hydrothermal features and the exciting small-scale eruptive activity. Such volcanic systems may appear to be safe, and decades may pass without an event that impacts visitors (Kilgour et al., 2021). However, small departures from the usual activity are possible, represented either by a small increase in eruption size, or due to a vent system

change that may locally increase the chance of a lateral mass flow or directed blast. Either process may have significant hazard/impact consequences to near vent visitors.

Eruptive directionality for small-scale systems have been increasingly observed in the past decade, due to improved observational capabilities from the global volcano monitoring community. Phreatic and phreato-magmatic eruptions at Ruapehu (Kilgour et al., 2010; Jolly et al., 2010), Te Maari (Lube et al., 2014; Jolly et al., 2014; Fitzgerald et al., 2014), and Ontake (Tsunematsu et al., 2016; Takarada et al., 2016) have all revealed significant hazards from lateral eruption events that have produced infrastructure damage or injuries and fatalities. Recent studies at Strombolian systems have also documented eruption directionality as evidenced by infrasound and ballistic mapping at Yasur volcano, Vanuatu (e.g., Jolly et al., 2017; Iezzi et al., 2019; Fitzgerald et al., 2020). Lateral directionality is not confined to small eruptions, however. Indeed, the 1980 Mount St. Helens blast (Kieffer, 1981; Kanamori and Given, 1982) produced significant lateral blast products from the syn-eruptive landslide event.

Eruption directionality is analogous to earthquake directivity and may suggest common wavefield propagation features. For a large earthquake, directivity results from rupture propagation within the fault plane which can produce variable waveform amplitude and spectral characteristics towards and away from the primary rupture direction (e.g., Eberhart-Phillips et al., 2003; Abercrombie et al., 2017) on a surrounding seismic network. Anthropogenic sources also may produce directivity/directionality features. In volcano observatory settings, helicopter or fixed wing aircraft (e.g., Hubbard et al., 1971) are often observed in seismic and acoustic records as tremor like signals having highly variable peak frequencies consistent with the Doppler spectral shift (Eibl et al., 2015).

Ballistic and ash particles, which may produce acoustic waves through turbulent interaction with surrounding air (Matoza et al., 2013; Rowell et al., 2014) can produce extended sources that may be recorded on nearby sensors. In this case, the excitations produced by the ash/ballistic mass may impart different frequency contents to a stationary observation point towards or away from the direction of eruption mass propagation. Consistent with this theory, one might expect to observe lower frequency signals for an acoustic sensor positioned behind the direction of propagation, and generally higher

frequencies for a sensor in the direction of mass flow.

In this contribution, we complete an initial controlled field-scale laboratory experiment where we attempt to create directionality features of vertical and laterally directed explosions. We aim to establish field conditions that emulate those captured by a set of acoustic sensors in the near-field (where the source dimension is large compared to the observation array) volcanic environment while controlling important features of an eruption, including the event size, source response and discharge direction, such that waveform features and spectral characteristics can be monitored. The eruption conditions emulated here are mixed liquid-gas jets (e.g., Zhang et al., 2016) that are akin to eruptions through volcanic lakes (e.g., Kilgour et al., 2010; Jolly et al., 2010; Fee et al., 2020; Lyons et al., 2019), and may be dynamically different from ash-gas jets from dry bed volcanic systems. Regardless, by controlling the eruption parameters, we aim to determine which characteristic features may be identified for real volcanic eruptions, to improve eruption source characterization and inform volcano monitoring decisions.

Results of this exploratory experiment show that efforts to control the source process were only partially successful as shown by the variations in waveforms event-to event. However, a subset of the highest energy explosions suggests that the acoustic impulse response from an artificial eruption imparts distinct spectral signatures that may emulate features of natural volcanic eruptions. The work provides a framework for improvement of future experiments of this class.

2. Experimental setup

We developed an experimental apparatus (Fig. 1) to produce directed explosions consistent with a prior field experimental eruption approach (Wadsworth et al., 2018). The setup included a 209-liter steel barrel (diameter 572 mm and height 851 mm) partially filled to ~1/3 capacity with water at approximately ambient temperature. For each experiment a light-duty plastic bottle (1.5-liter emptied soda-pop bottle) was filled to ~1/4 with liquid nitrogen (N_2), sealed with the cap, and immersed into the water. The process of immersion produced heating and gas expansion within the bottle which increased the internal bottle pressure. The bottles tensile strength was eventually exceeded, causing

bottle rupture and rapid expansion and vaporization of the liquid nitrogen. Our experimental design avoided the expense and logistical complexity of chemical explosive experiments (e.g., Goto, et al., 2001; Bowman et al., 2014; Sonder et al., 2022) allowing the generation of multiple example events over a relatively short period.

The resulting explosion was directed through the open end of the barrel (the vent) causing a directed blast of the water/liquid nitrogen mixture. The barrel was secured on a small truck trailer and the bottle was secured to the base of the barrel by a heavy mass with duct tape holding the immersed bottle in place (Fig. 1b and c). The barrel angle from vertical was adjustable via the natural angle of the trailer tow structure (Fig. 1d) augmented by stable wood support which in our case, allowed the explosion direction to be variably adjusted. Experiments included discharge angles of ~0°, 12° and 24° from vertical and azimuths northeast (70°) and southwest (250°) from true north. The experiment occurred on 3 March 2016 at Owen Delany Park in Taupo, New Zealand. Mild weather conditions were available with temperatures ~18°C and light variable winds that did not exceed ~4 m/s. A total of 12 experiments were attempted (Table 1), over a 2.5-hour period.

Data were collected using 9 infraBSU infrasound sensors (Marcillo et al., 2012) surrounding the apparatus at ranges of 2-70 m (Fig. 1a and Table 1) from the source. The acoustic data was collected on 3 DiGOS DATA CUBE digitizers recording at 200 Hz with cables to each sensor. The sensors had a flat response from 0.033 to 200 Hz and GPS locations were known to within ~5 m. The sensors were deployed to surround the cannon source position: three were positioned northeast of the source (ABZ0, ABZ1, ABZ2), three southwest of the source (AC20, AC21, AC22), two laterally on either side of the rotatable cannon (AC30, AC31) and one sensor (AC32) was located beneath the trailer (within ~2 m of the base of the cannon source position-SRC). A summary of the field setup is shown in Fig. 1a and Table 1 and 2. Video was recorded by three GoPro Hero 3 cameras, orthogonally oriented to the eruption to capture directionality and exit velocity. The GoPro cameras recorded at 30 frames per second and individual frames were extracted from the videos. In most cases, color was inverted to improve contrast, and the parabolic paths of balls with tracks most orthogonal to the camera angle were measured individually to get maximum velocities and heights (see Table 3 and

supplementary videos). Evening lighting and camera resolution provided some challenges with detailed tracking analysis. The measurements presented here focused on camera 2 and a comparison between experiment 9 vertical explosion and experiment 12 the 24° northeastward directed experiment. For this reason, only partial tracks for several ballistics were analyzed. Additionally, the velocity of the vaporized water and liquid nitrogen was tracked for these two experiments.

For infrasound sensors, we synchronized the data timing, corrected the data to pressure, extracted individual events and computed the spectra using standard Fast Fourier Transform (FFT) over a 200 sample (1s) window drawn from the unfiltered record. All waveforms are available as part of an online data release (see Availability of data and materials section).

3. Results

For the 12 experiments attempted, two failed to discharge due to slow bottle cap leakage (Table 1). Each of the 10 successful explosions was recorded on the 9-element ground network, however, Experiment 10 occurred during a very short data gap for sensor AC20 and that data was excluded from the analysis. For the successful discharges, three primary issues were noted. First, we found that the waveform data may have been under-sampled (Fig. 2) related to the 200 Hz data rate. Hence, the full wave features and spectral content of the discharges may not be fully captured. Second, a subset of the explosions had insufficient energy release based on the measured peak pressure at the near cannon sensor (AC32). Table 1 shows that the peak pressure at AC32 for the experiment ranged from 20.9 to 72.7 Pa (Fig. 2), but the aforementioned under-sampling implies that the true peak pressures may be higher. Inspection of the wider waveform and spectral data shows that the smaller events had significant low frequency noise (Fig. 3, 4 and 5). Third, Experiments 1, 2 and 6 produced complex spectral patterns (Fig. 4a, 4c and 5a) which were difficult to interpret.

With these issues, we limited the interpretation to events having peak pressures above 30 Pa at the near source station (AC32) and we did not interpret observations for events having multiple spectral peaks. Application of these criteria left 6 events (3, 5, 9-12)

for subsequent analysis. The subset of events included one vertical discharge, three northeast directed discharges, and two southwest directed discharges. Unfortunately, the southwest directed discharges did not include a high lateral angle example, limiting their value for the interpretation of lateral directionality. For completeness, we include all examples in (Fig. 4 and 5).

The selected events yielded two primary observations. First, despite the effort to control the discharge characteristics of the experiment, we obtain highly variable source excitations from event-to-event (Fig. 2). Second, despite these variable source-time histories, we observe systematic variation of the spectral contents for high-quality lateral and vertical blasts (Fig. 3, 4 and 5).

The near cannon spectral features carry over from the source (AC32 sensor within 2 m of the source SRC) to the outbound stations. Example waveforms and spectra for two events are shown in Fig. 3. These examples were selected because: 1) they had excellent signal-to-noise characteristics and a single broad spectral peak (2-80 Hz), 2) they represent two end member observations (both a vertical and laterally directed blast), and 3) the near source wavelets and spectra were similar for each event (Fig. 2). The waveform data for each event show approximately uniform wave pulses across the network and reveal characteristic under-sampled waveform features (Fig. 3a and b). However, the data have somewhat different event size which may contribute to the spectral observations.

For the vertically directed blast (Fig. 3a and c) the spectral characteristic on the surrounding network is strongly uniform regardless of the sensor aspect relative to the station. By comparison, the explosion having a strong lateral blast component (Fig. 3b and d), reveals systematic enrichment towards higher frequencies for sensors in the direction of the blast, and depletion of those frequencies behind the blast. The observed spectral distortion occurs at ~62 Hz for this example (see colored filled squares Fig. 3d). To illustrate the azimuthal features graphically, we plot the peak spectral frequency as a polar plot for both the vertical discharge (Fig. 3e) and the northeast directed lateral discharge (Fig. 3f).

We see that the other 24° northeastern blast (Experiment 11-Fig.5g and h) has somewhat similar features to Experiment 12 (Fig. 3d and f). For the smaller angle (near vertical) cannon discharges, (Experiments 3, 5 and 10 in Table 1) the systematics of lateral discharge components are not well resolved and in the case of experiment 10 (Fig. 5 e and f) are similar to Experiment 11 (Fig. 5g and h). These events, along with the single vertical discharge show more uniform spectral patterns (compare Figs. 4e, 4g and 5e to Fig. 3c). The only southwestern directed example shows a modest frequency enrichment in the direction of the blast is seen in Experiment 5 (Fig. 4g) which has weakly enriched frequencies above 60 Hz (compare northeastward sensors (red lines) to southwestward sensors (blue lines)). Given the potential under-sampling discussed above, interpretation of higher frequency observations for this experiment should be undertaken cautiously. This assessment is completed in Section 4.2.

The video observations from experiment 9 show a narrow vertical explosion with a limited ballistic distribution range (~10 m). In contrast, experiment 12 has a northeast directed outward fanning explosion and larger northeasterly distributed ballistic range (~15 m) (see supplemental images). In all experiments, the initial measured maximum velocity of the vapor jet was higher than the subsequent measured maximum velocity of the ballistics. Experiment 9 shows that the vapor jet was higher velocity (60.0 m/s) compared to experiment 12 (28.3 m/s), consistent with the higher initial pressure calculated from the infrasound (Fig. 2), however the balls from the two experiments had similar maximum measured velocity ranges (Table 3).

4. Discussion

Our results reveal highly variable source excitations from event-to-event (Fig. 2) and systematic frequency partitioning for individual events (Fig. 3c and d). These observations have implications for the interpretation of source processes that occur in a wide range of observational settings including the interpretation of repetitive sources found in both natural acoustic and seismic data (e.g., Danesi et al., 2007; Park et al., 2019).

Our experimental setup produces a source that has conceptual similarity with prior work

in volcano-acoustics. For example, Buckingham and Garces (1996) presented a canonical model of volcano acoustics, providing an analytic solution for the upgoing sound field from a resonant magma (or gas-filled) conduit, with the trigger-mechanism pressure excitation function provided by a bubble pulse airgun-like source signature at depth in the conduit. We also have a submerged bubble expansion source, but in our case the wavelength of the bubble oscillations presumably approach or exceed those of the barrel container, and the bubble expansion is shallow enough that the full bubble pulse oscillations are not completed before the material is ejected. Thus, our source is more complicated than a deeper more pressure confined air-gun-like source (Buckingham and Garces, 1996). Ichihara et al. (2009) discusses a related case of lake water surface explosions (not confined by conduit walls). In addition, our source is conceptually similar to the directed blast numerical simulations of Watson et al. (2021). We note that Watson et al. (2021) observed enhanced high frequencies in the downstream blast direction (i.e., above the vertically directed source), consistent with our observations.

4.1. Variation of a repeating source

While we attempted to produce identical acoustic impulses event-to-event, strong variations in waveforms and spectra for the ten events testify to an unstable source process. This is remarkable, considering that the source location was stationary relative to the sensor array and our methodology attempted to produce a uniform source discharge. Even repeat discharges with the same cannon orientation (Experiment 11 and 12) produced somewhat different waveform and spectral characteristics (See Figs 2, 3 and 5).

In natural systems, the observed waveform is interpreted to be dominantly impacted by four elements: the source, path, site and instrument. If the source mechanism is identical for two or more events at a stationary position, then the resulting waveforms would be highly similar because each of the four elements would be nearly constant over short inter-event times (e.g., Green and Neuberg, 2006; Park et al., 2019) related to a constant eruption trigger, barrel geometry, water fill level and barrel opening producing highly similar waveforms and spectra. In this context, if we return to the multi-peaked spectra for events 1, 2 and 6 (Fig. 4 and 5), the observed spectral peaks might hypothetically be related to a path effect associated with a Lloyd mirror (e,g., Carey, 2009) where direct

292 and ground reflected waves might be superimposed to produce constructive and
293 destructive wavelets dependent on the distance from the source. In our case, however,
294 the peaks persist for all stations consistent with a source rather than path effect. Instead,
295 the systematic similarity of all spectra for a given experiment (Fig. 4a, 4c and 5a) suggest
296 that the source is dominating the spectra and that some features experiment-to-experiment
297 are unconstrained and highly variable.
298
299 We suggest that the non-systematic features of the experiment-to-experiment source
300 process may relate to non-uniform strength characteristics of each plastic bottle as well
301 as small variations in the position of the bottle at the base of the barrel. We also surmise
302 that rapid bottle rupture would displace the bottle laterally along the base of the barrel in
303 a somewhat random manner. The bottle rupture process may introduce unconstrained
304 energy directivity effects. In addition, while we attempted to control the capacity of
305 liquid nitrogen (N_2) into each bottle, prior experiments (e.g., Wadsworth et al., 2018 and
306 other unpublished experiments including a subset of our team) showed that larger
307 volumes of N_2 increased the explosion yield. We estimate errors in N_2 bottle fill and
308 water barrel fill to be within 5%, while the barrel inclination is known to within a couple
309 of degrees. Finally, we note that the inclination of the barrel would produce distortions
310 in the water height relative to the source depth. Together, these small variations
311 probably contributed to the non-repeating rupture-time histories and attendant variation
312 in the spectral characteristics.
313
314 In addition to the highly variable source-time histories, careful inspection of Fig. 2
315 suggest that waveforms may also be systematically evolving through time. We consider
316 two aspects of the experiment that might contribute to the evolution of the waveform
317 features. First, the bottle type was changed after the sixth experiment when the supply
318 of L&P type bottles was exhausted. Later explosions had generally greater
319 overpressures (Table 2) and we surmise that the MY bottles used for experiments 6-12
320 failed at higher internal pressure thereby initiating the expulsion event with gas at a higher
321 pressure. Second, over the progression of the experiment, the plywood floor of the
322 trailer began to fracture and deform. By the end of the experiment the floor rested on
323 the steel under-structure which was also progressively deformed (Fig. S1). We regard
324 this slow destruction of the cannon's trailer frame as an analog to a destructive source

process in nature although the temporal variability is difficult to constrain in our case. For the natural system, this might be equivalent to the progressive erosion of an active eruption vent (e.g., Fee et al., 2016; McNeil et al., 2018), or the progressive rupture around a repeating subsurface earthquake source (e.g., Park et al., 2019), although the experimental destructive process is not scaled, and little is known about the destructive source processes in natural systems. We regard these aspects of the experiment as the primary contributions to the large observational changes event-to-event. It is clear that care must be taken before ascribing source stability, or progressive variations to one process or another (e.g., Park et al., 2019).

4.2. Source directivity

Moving next to the systematic aspects of the frequency content for each event, we first examine if we have completely sampled the spectral content and, if not, what is the upper frequency that can be faithfully interpreted? For several seismic studies in volcanic settings, the interpretation is undertaken in the 2-25 Hz range for data sampled at 100 Hz (e.g., about 50% of the corresponding Nyquist frequency of 50 Hz) (e.g., Hotovec et al., 2013). In volcano observatory settings, helicopter and fixed wing aircraft noise is also commonly observed at frequencies >10 Hz, and detailed assessments have resolved persistent signals as high as 35 Hz (Eibl et al., 2015) corresponding to about 70% of Nyquist. From this, one could anticipate that frequencies of ~70 Hz might be resolved in our 200 Hz data. However, frequency characteristics of a more persistent 'tremor like' source (e.g., a helicopter) may be easier to resolve than the short-duration impulses recovered here. Higher frequency observations may correspond to very few data samples for a given waveform in our specific case. In addition, higher frequencies might be impacted by digitizer related anti-alias filters. To assess this, we compared gain corrected observations to poles-and-zeros restitutions to assess the high frequency roll-off in the data (Fig. S2 and S3). Inspection of waveforms and spectra show that amplitudes and frequency distortions are only seen at frequencies <~5 Hz, as expected from the nominal response curve (Fig. S4).

These considerations suggest that the frequency content of near field acoustic sensors may be interpreted with reasonable confidence below about 70 Hz. The observed

enrichment-depletion occurs around 40 to 70 Hz for our highest quality observations (Experiments 5, 9, 10, 11 and 12 in Fig. 2, and Fig. 4, 5 and 6) while observations above 70 Hz (e.g., Experiment 5-Fig. 5g) are probably on the edge of our ability to interpret. We emphasize here the small number of experimental observations and the high variability observed event-to-event; hence a strong interpretation of the results is not possible in our case. With these caveats, we next consider the range of mechanisms that might produce the frequency enrichment observations.

The overall source dynamics for acoustic sources has been developed from early work by Woulff and McGetchin (1976) and Lighthill (1978) and consists of monopole (explosive) sources, dipole (bi-directional) sources and multipoles (superimposed combinations of dipole sources). Combinations of these source types are generally consistent with volcanic eruptions (e.g., Iezzi et al., 2019; Kim et al., 2012) and are likely to match the observations for our experiments. In this context, we may consider the outcomes of our experiments with equivalent source representations that approximate monopole and dipole source processes (e.g., a complex source mechanism) related to directed explosions. Extending from this, we consider two possibilities for the azimuthal enrichment: 1) frequency enhancement due to a Doppler shift of an extended source process (the source and its extended plume), or 2) a diffraction of acoustic wave energy due to the obstruction of the cannon barrel and trailer bed. Other contributions to variable source spectral observations might include variable water height in the inclined barrel or systematic shifts in the explosive source at the base. Such effects are hard to assess within this contribution and are not considered further.

4.2.1. Plume energetics and the Doppler shift

In the first case, we assume that the acoustic source propagates at subsonic speeds and that the source includes both the initial rupture and expansive discharge, but also a distributed source component representing the ejected plume. The acoustic source is confined and directed from the barrel itself and propagates outward with an efficiency related to the visco-elastic barrel base and walls as well as the opening. We envisage that the barrel is the primary source, but the mass of the ejected fluids may produce acoustic signals by plume turbulence (e.g., Matoza et al., 2009; Matoza et al., 2013).

From an observational perspective water, N_2 gas and colored balls are clearly directed by the barrel orientation. The system may be analogous to water/gas explosions in laboratory settings (Ichihara et al., 2009; Zhang et al., 2016) and also for acid lake hydrothermal eruptions (e.g., Caudron et al., 2018; Jolly et al., 2018). We hypothesize that this system would produce enriched frequencies in the direction of plume propagation, and depleted frequencies behind the plume.

To test this hypothesis, we examined the discrete motions of discharged particles using methods outlined in Jolly et al. (2016). For this purpose, we tracked both individual-colored balls contained in the water as well as individual steam propagation fronts using video data. For the balls, the estimated velocity was about 10-20 m/s while the water splash and N_2 gas mixture was found to have a velocity around 28-60 m/s. We note that the balls have lower density and larger volume compared to the individual water splashes mixture, producing increased frictional drag that likely contributed to their observed lower maximum velocities. It is also worth noting that the balls tended to be measured farther along their trajectories away from the source, whereas the water gas jet was measured closer to source (See supplementary videos and Table 3).

Restricting our analysis to the steam propagation and assuming that the plume is the source of mass propagation producing the full infrasound waveform, we use the standard formulation for the Doppler shift, $F_t=f_o(C+V_r)/(C-V_s)$, for propagation towards the observation point, and $F_a=f_o(C-V_r)/(C+V_s)$, for propagation away from the observation point. Here f_o is the frequency of the source, V_s is the velocity of the propagating source, V_r is the velocity of the stationary receiver (0 m/s), C is the acoustic velocity which is assumed 345 m/s. Because the angled source includes both vertical and lateral velocity components, we apply a Cartesian correction to obtain the lateral component along the Earth's surface. For the maximum amplitude for Experiment 12 (f_o ~45 Hz at the near source station AC32) we obtain F_a = 43.5 Hz and F_t = 46.6 Hz. The observed range of frequencies is 43 Hz (blue lines in Fig. 3d) and 73 Hz (red lines in Fig. 3d). While the theoretical Doppler shift is of the correct polarity and may partially contribute to the observations, the Doppler related frequency distortion is not sufficient to produce the acoustic observations in Fig. 3. While it is likely that the discharge velocities within the cannon barrel are more than those observed in the video, a Doppler shift cannot fully

explain the observations for Experiment 12.

4.2.2. Wave diffraction and frequency content

An alternative hypothesis is that the cannon and trailer may produce a natural barrier to the propagation of acoustic energy within the sampled frequency range (e.g., Kim et al., 2012). For a vertical discharge, all frequencies are propagated uniformly, producing the observations shown in Fig. 3c. With increased lateral discharge, the sensors open to the barrel would have no barrier to the full spectral content of the discharge, while sensors laterally and behind the cannon would record diffracted acoustic signals, with these effects being more pronounced at higher frequencies. In this case, the laterally directed energy from the barrel would produce some recoil energy that is partially absorbed and distributed by the barrel walls, trailer, and other elements like rubber wheels, shock absorbers and the ground. We observed recoil and barrel bounce associated with all discharges, and distinct late arriving acoustic transients at the near source station (see Fig. S5). While we were able to document lag times from the video records that may relate to pressure transients at the near source sensor (AC32), a lack of absolute timing for video records implies inexact measurement of lag times. Regardless, we find lag times from 0.2 (experiment 5) to 0.9 s (experiment 9) after the visible initiation of the experiment.

It is difficult to test the wave diffraction hypothesis, without application of synthetic waveform modelling incorporating elastic or visco-elastic boundaries. While modelling for directed sources in active volcanoes has been completed based on a stationary source with directionality represented by a force vector (e.g., Iezzi et al., 2019), such modelling would be difficult to implement in our case given the scale issues and complexity of the apparatus. Regardless, we surmise that both the extended distributed source model, and the visco-elastic barrier model likely contribute to our observations.

5. Conclusions and implications

This work highlights the observations from vertical and laterally directed explosions from an experimental apparatus designed to emulate natural phenomena from volcanic eruptions. Our primary observations include strongly variable source time functions for

457 waveforms and spectra as part of a spatially distributed source process and frequency
458 enrichment/depletion profiles associated with laterally directed blast events.
459
460 Limitations in the initial experimental design have been highlighted to aid the
461 interpretation of the data as well as to highlight possible improvements to future
462 experiments of this type. Amongst these, we note the possible under-sampling of the
463 experiment and its potential impacts on our interpretations. Whilst we acknowledge that
464 the observed waveforms and spectra may not represent the full wavefield, we note that
465 the observations are systematically seen on multiple stations and azimuthal directions.
466 In this regard, future experiments of this type should increase the sampling rate to at least
467 400 Hz. Whilst this is within the specification for the infraBSU and CUBE digitizer,
468 microphone-based recording may improve resolution of high frequency components. In
469 addition, application of a different cannon design might improve the observational range
470 that could be assessed. For example, use of a cannon apparatus incorporating solid
471 chemical explosive sources (e.g., Goto et al., 2001; Bowman et al., 2014; Sonder et al.,
472 2022), could produce more uniform discharges at greater inclinations. While the use of
473 chemical explosives increases logistical complexity and expense, they would allow
474 assessment of 'dry bed' lateral eruption dynamics. Dry-bed eruptions might also be
475 simulated using the same liquid nitrogen charged cannon but excluding the confining
476 water column. Further, denser observation including more acoustic sensors at a greater
477 range of azimuths and incidence angles, would potentially allow incorporation of more
478 sophisticated modelling approaches as well as the application of source inversion.
479 While such approaches may be beyond the applicability of the present data, a new
480 experiment including dense ground and aerial deployments (e.g., Jolly et al., 2017) could
481 allow a more rigorous assessment of extended source processes. In addition, it would
482 be useful to incorporate video records having absolute timing, as this would improve
483 assessment of late-stage secondary pulses (Fig. S5). The largest secondary pulse, for
484 experiment 6, was observed clearly across all sensors in the local network.
485
486 Results from this experiment illustrate that variations in the energy release from angled
487 explosions can be captured in acoustic sensors surrounding volcanic systems. The
488 observed acoustic spectra varied considerably between experiments despite similar
489 experimental setups and an effort to have a repeatable source, suggesting that small

490 changes in source dynamics can produce large observed changes in the acoustics in this
491 experimental setup. While the observations were collected from very near source, where
492 the source dimension is large compared to the observation network, they offer an
493 immediate applicability to improved volcano eruption assessments. In particular, the
494 results highlight the potential for dense near-field capture of volcanic eruption data for
495 frequently active phreatic or Strombolian systems, where localized hazards may be
496 present. Such observations may enable the development of improved hazards zones for
497 emergency managers, and improved eruption detection systems for volcano monitoring
498 akin to mass motion monitoring systems for lahar monitoring systems (e.g., Sanderson et
499 al., 2021).
500

Figure legends

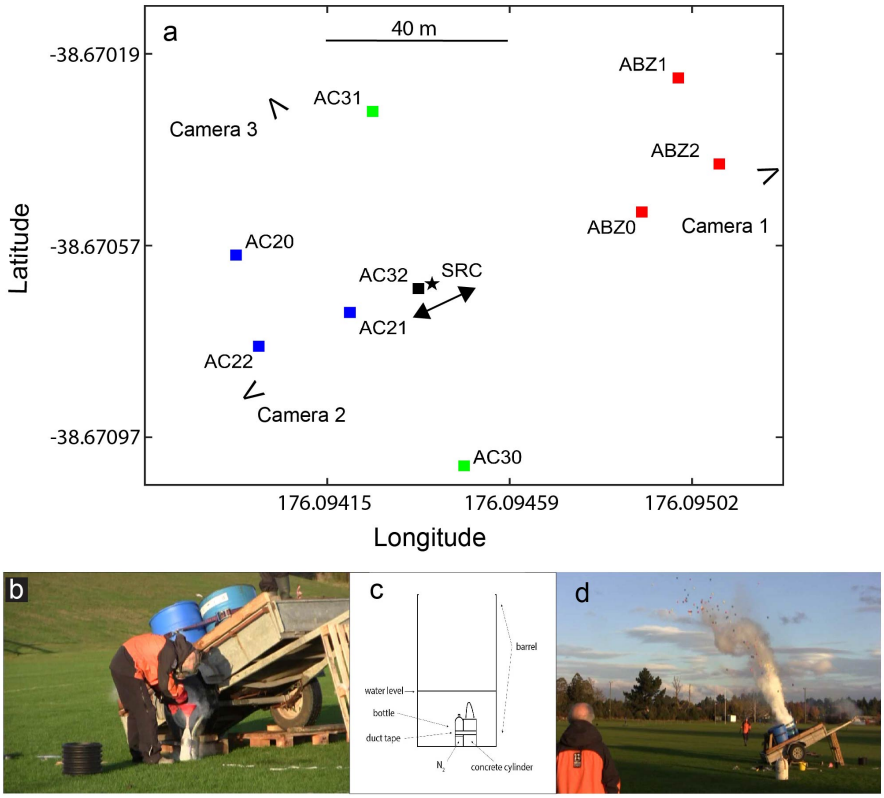

Fig. 1: Map (a) showing experimental set-up and distribution of sensors (squares colored red for northeast sensors, blue for southwest sensors, green for sensors lateral to the discharge direction and black for a sensor under the cannon). The angled blast direction is shown by the black double arrow. Latitude and longitude are given in decimal degrees. Cameras (V open to the look direction) documented 10 successful discharges. The black star shows the cannon. For each experiment, the bottle (b) was partially filled with liquid-nitrogen, sealed with the cap and placed in the partially water filled barrel (see section 2). Diagram showing the discharge apparatus within the barrel shown in (c). An example discharge (d) for Experiment 11 yielded a lateral discharge of a water/nitrogen mixture. Colored balls aided assessment of discharge exit velocities. Images (b and c) are from video captures generated by Julian Thompson (GNS Science).

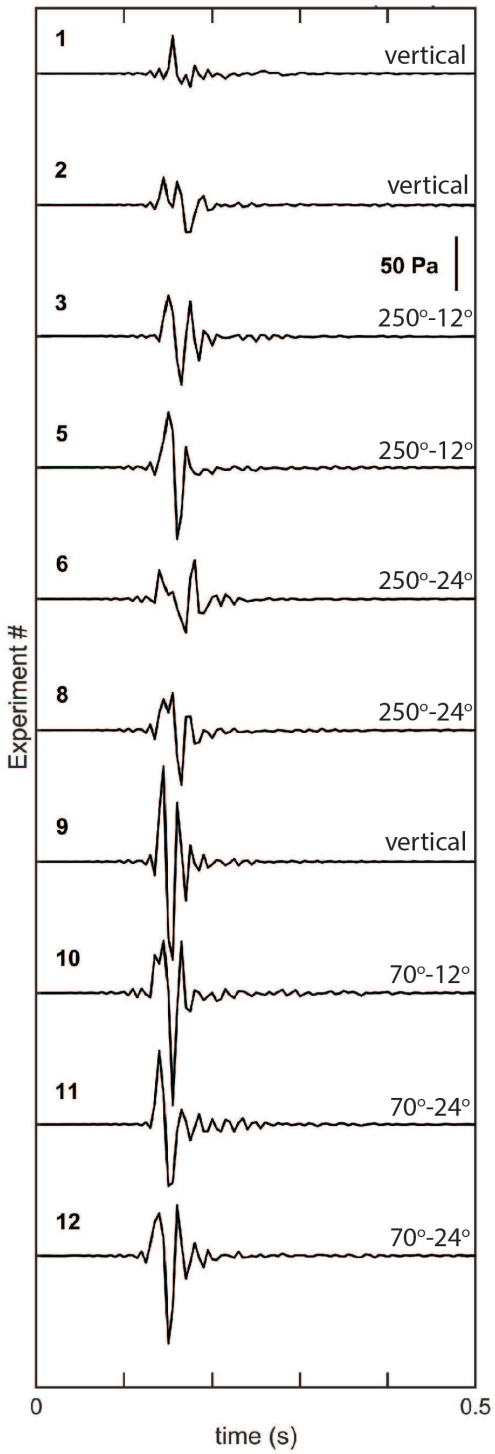

Fig. 2: Example discharges from sensor AC32 located under the source (SRC). Each discharge is labeled as described in Table 2. Note the highly variable waveform characteristics event-to-event. The window onset is ~0.1s prior to the explosion onset for each experiment.

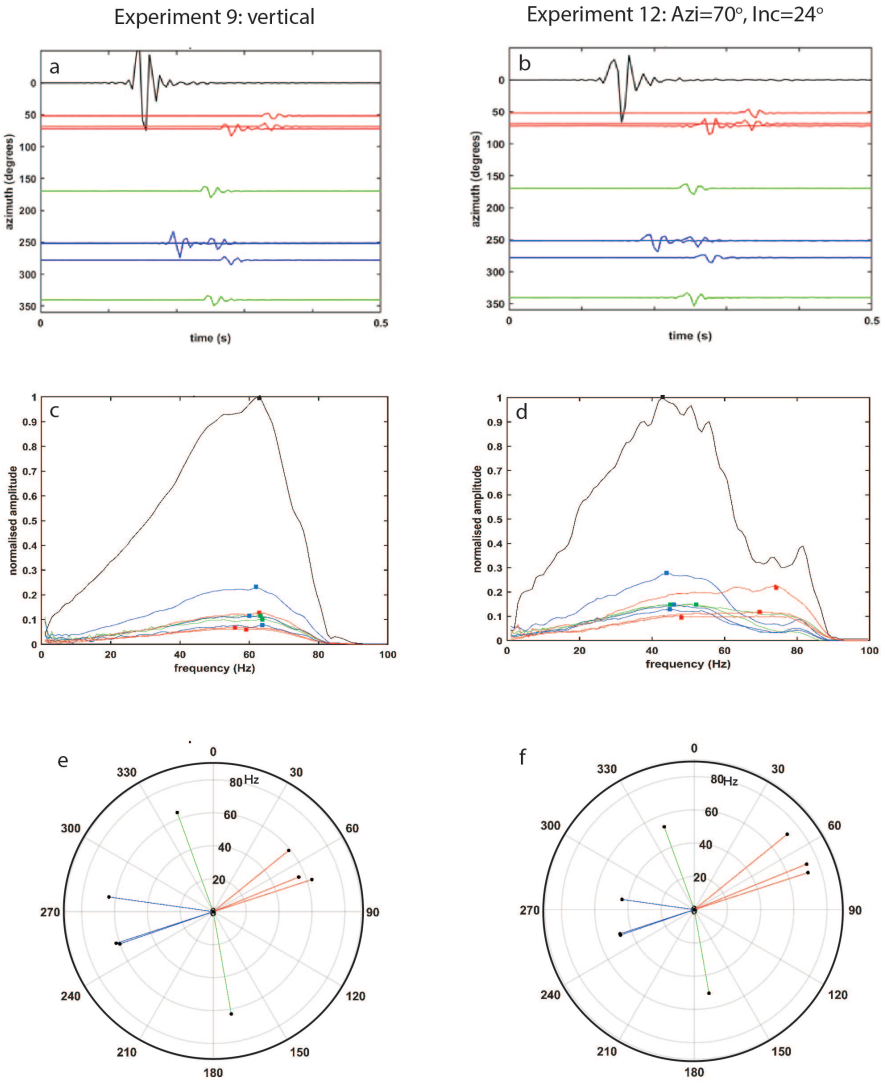

Fig. 3: Example acoustic waveforms (a and b) and spectra (c and d) for vertical (a and c), and north-east directed (b and d) blasts. Color is representative of the station distribution in Fig. 1. Example polar plots (e and f) show peak spectral frequencies (0 to 100 Hz with low frequencies in plot center) and station azimuth (1-360° clockwise from North at the top) relative to the source position (SRC). Squares mark maximum frequency of each spectra as shown (e and f) note for lateral discharge shown in d and f the higher frequencies northeastward and diminished frequencies southwestward. The window onset for a and b is ~0.1s prior to the explosion onset for each experiment.

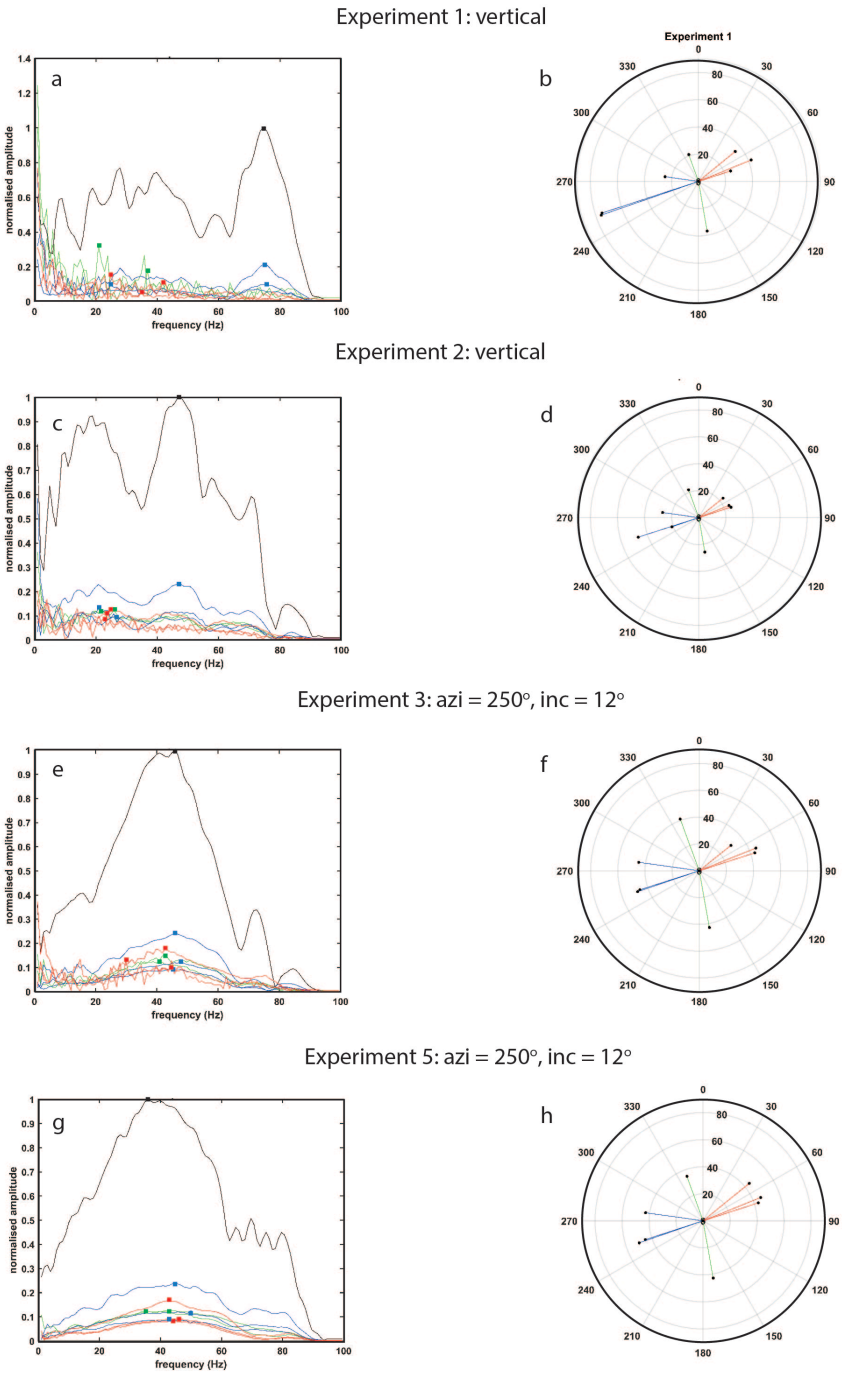

Fig. 4: Complete analysis of eruption data for experiments 1, 2, 3, and 5 following analysis from Figure 3.

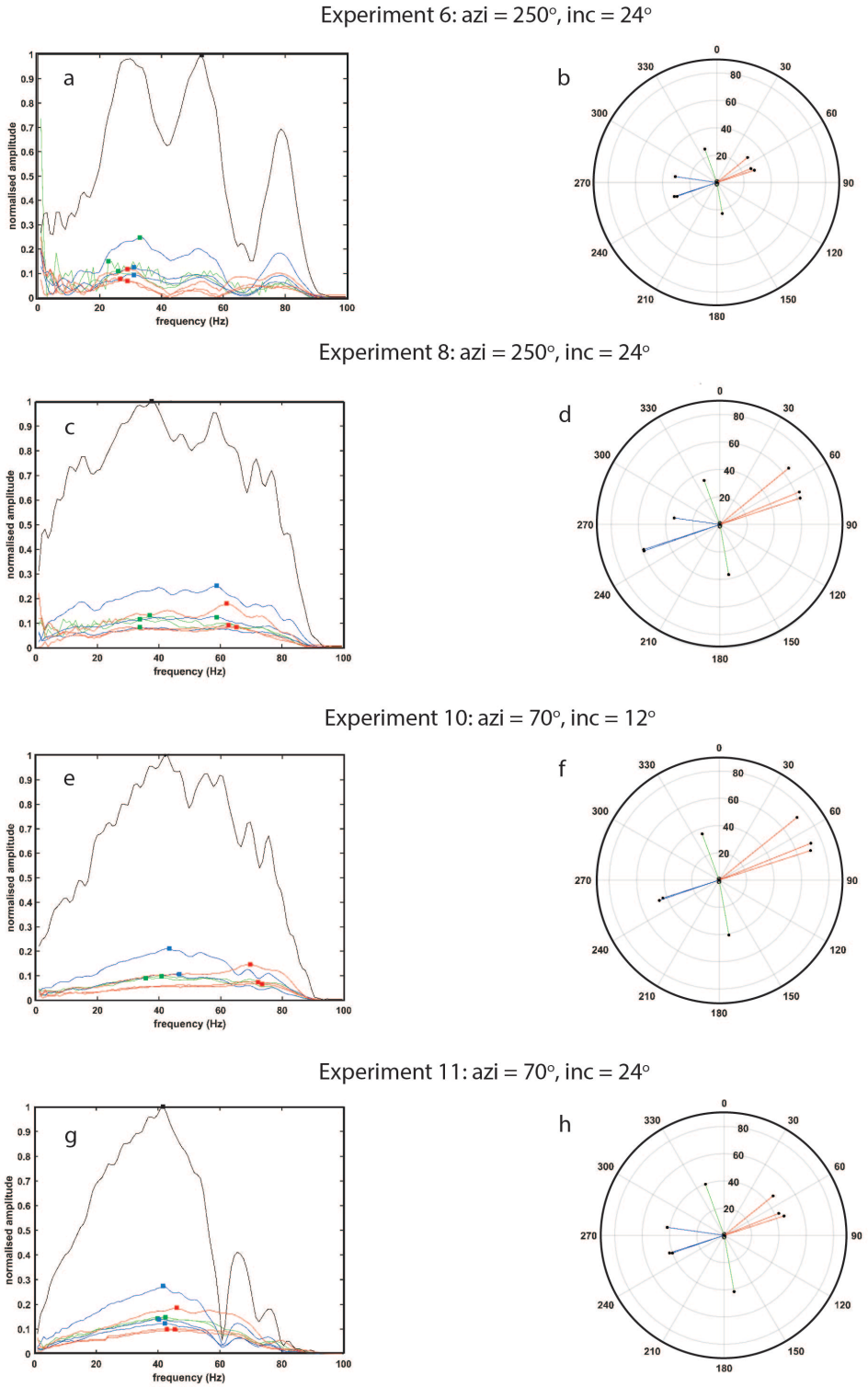

Fig. 5: Complete analysis of eruption data for experiments 6, 8, 10 and 11 following analysis from Fig. 3.

a) Experiment 9: vertical

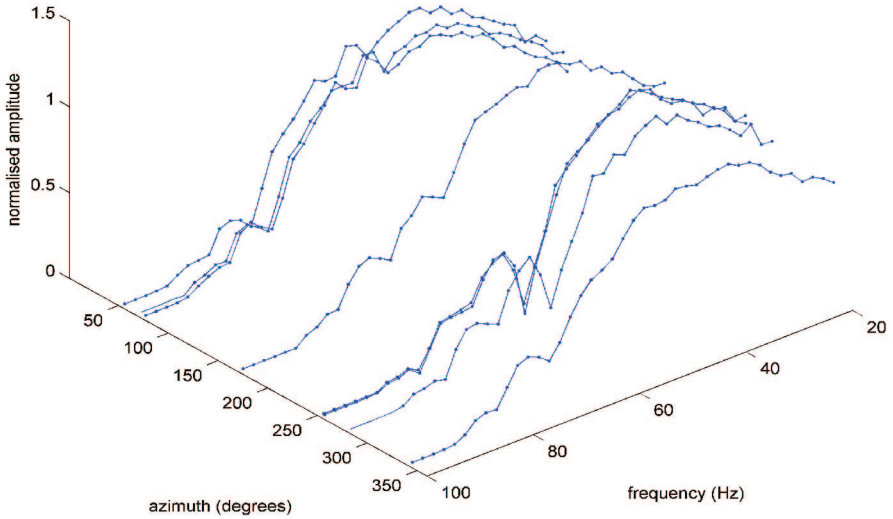

b) Experiment 12: Azi=70°, Inc=24°

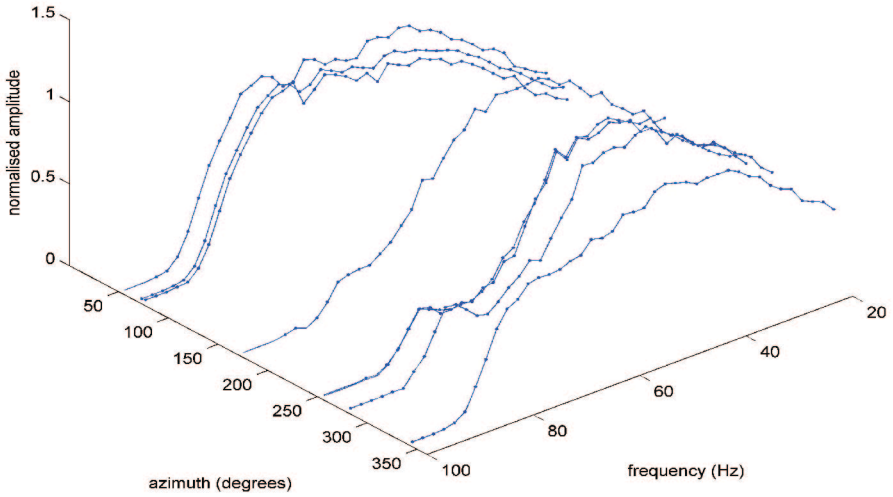

537

538 Fig. 6: Azimuthally grouped spectra for (a) Experiment 9 and (b) Experiment 12

539

540

541

Table 1: Experiment results. Bold denotes interpreted experiments.

N	Event time (UTC)[1]	azimuth[2]	blast angle[3]	pressure (Pa)[4]	comment[5]
1	02:26:45	Vertical	0°	28.8	L&P
2	02:35:49	Vertical	0°	20.9	L&P
3	**02:47:41**	**250°**	**12°**	**31.2**	**L&P**
4					failed discharge
5	**03:26:24**	**250°**	**12°**	**42.3**	**L&P**
6	03:51:41	250°	24°	29.4	L&P
7					failed discharge
8	04:13:48	250°	24°	28.6	MY
9	**04:21:40**	**Vertical**	**0°**	**72.7**	**MY**
10	**04:35:04**	**70°**	**12°**	**39.8**	**MY**
11	**04:50:12**	**70°**	**24°**	**56.1**	**MY**
12	**04:57:21**	**70°**	**24°**	**38.6**	**MY**

[1]Experiment date is 3 May 2016 14:26 to 16:57 NZST (3 May 2016 2:26 to 4:57 UTC).

[2]Measured clockwise from north.

[3]Measured from vertical.

[4]Peak positive pressure measured from beneath the explosion source.

[5]Bottle type detonated: (L&P) brown soft-drink bottles, (MY) clear soft-drink bottles.

560

561 **Table 2:** Station and cannon (SRC) latitude and longitude locations given in decimal
562 degrees.

Station	Easting (m)	Northing (m)	Elevation (m)	Distance (m)	Azimuth (degrees)	Comment
SRC	-38.670650	176.09436	395	0		Source position
AC30	-38.67098	176.09450	398	39	170	Lateral from source
AC31	-38.67032	176.09423	396	38	340	Lateral from source
AC32	-38.67065	176.09436	395	3	251	Under source
AC20	-38.67060	176.09390	391	43	278	Southwest of source
AC21	-38.67070	176.09419	392	19	252	Southwest of source
AC22	-38.67077	176.09397	392	40	251	Southwest of source
ABZ0	-38.67049	176.09492	398	48	72	Northeast of source
ABZ1	--38.67024	176.09500	400	69	51	Northeast of source
ABZ2	-38.670400	176.09511	400	67	58	Northeast of source

563

564

565

566

567

568

569 Table 3: Eruption description

	Max. measured vapor velocity (m/s)	Max. measured vapor height (m)	Max measured ball velocity(m/s)	Max measured ball height (m)*	Explosion description
Exp 9 (vertical)	60 (n=2)	6.3m	12.2-15.3(n=5)	9.4m	Vapor jet narrow vertical explosion, most balls went height and landed close to barrel, slight asymmetric distribution (northeast)
Exp12 (24 °)	28.3 (n=3)	5.1m	10.6- 21.7 (n=7)	4.5m	Fanned vapor jet, balls landed farther from barrel strongly asymmetric distribution (northeast)

570 *Measured from base of explosion above ground.

Declarations

The authors *must* provide the following sections under the heading "Declarations".

Ethics approval and consent to participate

Not applicable

Consent for publication

This publication has been peer reviewed and approved for publication consistent with U.S. Geological Survey Fundamental Science Practices (https://pubs.usgs.gov/circ/1367/).

List of abbreviations

Not applicable

Availability of data and materials

Acoustic and video data used in this study are available as supplemental downloads including:

Four gifs are supplied from camera 2, two for each experiment (both the tracked vapor jet and the tracked balls). Inverted color images in most cases provided the best contrast except for in the case of tracking the vapor jet in experiment 12 due to lighting.

And raw video footage is available on the ScienceBase open access service: Jolly, A.D., and Kennedy, B., 2022, Video Data for Cannon Discharge Events - May 3, 2016 - Taupo, New Zealand: U.S. Geological Survey data release, https://doi.org/10.5066/P92KGW4S.

Waveform data are available through the IRIS temporary network code 7L. https://www.fdsn.org/networks/detail/7L_2016/

Competing interests

Arthur D. Jolly is a member of the EPS editorial board and is blinded to the editorial process. The other authors declare that they have no competing interests.

Funding

New Zealand Ministry of Business, Innovation and Employment (MBIE) who supported AJ (formerly with GNS Science), BK, BC, RJ and CA and the New Zealand MBIE funded program Resiliency to Natures Challenges for support of BK and AJ (formerly with GNS Science). NSF Grant EAR-1952392 supported AMI.

Authors' contributions

AJ and BK conceptualized the experiment. RJ provided engineering and logistical support. AJ, BK, BC and RJ conducted the experiment. AJ, RM and AI processed and analyzed the acoustic data. AS, BK and AJ analyzed the video records. All authors supported the writing and approved the final manuscript.

Acknowledgements

We acknowledge the New Zealand Ministry of Business, Innovation and Employment (MBIE) who supported AJ (formerly with GNS Science), BK, BC, RJ and Cam Asher and the New Zealand MBIE funded program Resiliency to Natures Challenges for support of BK and AJ (formerly with GNS Science). RSM acknowledges NSF

grant EAR-1847736. NSF Grant EAR-1952392 supported AMI (UCSB). DF acknowledges support from NSF Grant EAR-1901614. Julian Thompson and Cam Asher provided video support of the project (GNS Science). We thank Leighton Watson for discussion about numerical simulations of explosions and Iseul Park for discussions around response correction for acoustic data. This manuscript was improved by reviews by Alicia Hotovec-Ellis and two anonymous reviewers. Finally, we thank handling editor Mie Ichihara for guiding the submission and very useful suggestions to improve the manuscript. Any use of trade, firm, or product names is for descriptive purposes only and does not imply endorsement by the U.S. Government.

Authors' information

Author #1: Arthur Jolly, 1) U.S. Geological Survey, Hawaiian Volcano Observatory, Suite A8, 1266 Kamehameha Avenue, Hilo, HI, 96720 USA, ajolly@usgs.gov; 2) GNS Science, 1 Fairway Drive, Avalon, Lower Hutt 5010, New Zealand

Author #2: Ben Kennedy, University of Canterbury, Department of Geological Sciences, Christchurch, New Zealand , ben.kennedy@canterbury.ac.nz

Author #3: Robin S. Matoza, Department of Earth Science and Earth Research Institute, University of California, Santa Barbara, CA, USA, rmatoza@ucsb.edu

Author #4: Alexandra M. Iezzi, Department of Earth Science and Earth Research Institute, University of California, Santa Barbara, CA, USA, amiezzi@ucsb.edu

Author #5: Bruce Christenson, [5]GNS Science, Avalon, New Zealand, b.christenson@gns.cri.nz

Author #6: Richard Johnson, Wairakei Research Centre, 114 Karetoto Rd., Wairakei, New Zealand, r.johnson@gns.cri.nz

Author #7: Amilea Sork, University of Canterbury, Department of Geological Sciences, Christchurch, New Zealand

Author #8: David Fee, Alaska Volcano Observatory, Geophysical Institute, University of Alaska-Fairbanks, USA, dfee1@alaska.edu

Indicate the corresponding author: Arthur Jolly

Endnotes

Not applicable

References

Abercrombie RE, Poli P, Bannister S (2017) Earthquake directivity, orientation, and stress drop within the subducting plate at the Hikurangi margin, New Zealand. J Geophys Res: Solid Earth 122, 12,176–10,188, doi:10.1002/2017JB014935

Bowman DC, Taddeucci J, Kim K, Anderson JF, Lees JM, Graettinger AH, Sonder I, Valentine GA (2014) The acoustic signatures of ground acceleration, gas expansion, and spall fallback in experimental volcanic explosions. Geophys Res Letts 41:1916–1922. doi:10.1002/2014GL059324

Buckingham MJ, Garcés MA (1996) Canonical model of volcano acoustics. J Geophys Res 101(B4): 8129– 8151. doi:10.1029/95JB01680

Carey WM (2009) Lloyds Mirror-Image Interference Effects. Acoust Today, April, 14-20

679
680 Caudron C, Taisne B, Neuberg J, Jolly AD, Christenson BW, Lecocq T, Suparjanh,
681 Syahbana D, Suantika G (2018) Anatomy of phreatic eruptions. Earth Planets Space
682 70:168. doi: 10.1186/s40623-018-0938-x
683
684 Danesi S, Bannister S, Morelli A (2007) Repeating earthquakes from rupture of an
685 asperity under an Antarctic outlet glacier. Earth Planet Sci Letts 253:151–158. doi:
686 10.1016/j.epsl.2006.10.023
687
688 Eberhart-Phillips D, and others (2003) The 2002 Denali Fault Earthquake, Alaska: A
689 Large Magnitude, Slip-Partitioned Event. Science 300 (5622). doi:
690 10.1126/science.1082703
691
692 Eibl EPS, Lokmer I, Bean CJ, Akerlie E, Vogfjord KS (2015) Helicopter vs. volcanic
693 tremor: Characteristic features of seismic harmonic tremor on volcanoes. J Volcanol
694 Geotherm Res 304:108-117. doi: 10.1016/j.jvolgeores.2015.08.002
695
696 Erfurt-Cooper P (ed), (2014). Volcanic tourist destinations. Springer.
697 doi: 10.1007/978-3-642-16191-9
698
699 Fee D, Haney MM, Matoza RS, Van Eaton AR, Cervelli P, Schneider DJ, Iezzi AM
700 (2016) Volcanic tremor and plume height hysteresis from Pavlof Volcano, Alaska.
701 Science 355:6320:45-48. doi: 10.1126/science.aah6108
702
703 Fee D, Lyons J, Haney M, Wech A, Waythomas C, Diefenbach A K, and others (2020).
704 Seismo-acoustic evidence for vent drying during shallow submarine eruptions at
705 Bogoslof volcano, Alaska. Bull Volcanol 82(1):2. doi: 10.1007/s00445-019-1326-5
706
707 Fitzgerald RH, Tsunematsu K, Kennedy BM, Breard E, Lube G, Wilson TM, Jolly AD,
708 Pawson J, Rosenberg MD, and Cronin SJ (2014) The application of a calibrated 3D
709 ballistic trajectory model to ballistic hazard assessments at Upper Te Maari, Tongariro. J
710 Volcanol Geotherm Res 286, pp. 248–262. doi: 10.1016/j.jvolgeores.2014.04.006.
711

712 Fitzgerald RH, Kennedy BM, Wilson TM, Leonard GS, Tsunematsu K, Keys H (2017)
713 The Communication and Risk Management of Volcanic Ballistic Hazards Advances in
714 Volcanol. Springer International Publishing pp. 121–147. doi: 10.1007/11157_2016_35
715
716 Fitzgerald RH, Kennedy BM and others (2020) Volcanic ballistic projectile deposition
717 from a continuously erupting volcano: Yasur Volcano, Vanuatu. Volcanica 3(2):183 –
718 204. doi: 10.30909/vol.03.02.183204
719
720 Green DN, Neuberg J (2006) Waveform classification of volcanic low-frequency
721 earthquakes swarms and its implication at Soufrière Hills Volcano, Montserrat.
722 J Volcanol Geotherm Res 153 (1–2):51–63. doi: 10.1016/j.jvolgeores.2005.08.003
723

724 Goto A, Taniguchi H, Yoshida M, Ohba T, Oshima H (2001) Effects of explosion energy
725 and depth to the formation of blast wave and crater: Field Explosion Experiment for the
726 understanding of volcanic explosion. Geophys Res Letts 28: 22: 4287-4290. doi:
727 10.1029/2001GL013213
728
729 Hotovec AJ, Prejean SG, Vidale JE, Gomberg J (2013) Strongly gliding harmonic
730 tremor during the 2009 eruption of Redoubt Volcano. J Volcanol Geotherm Res 259:
731 89–99. doi: 10.1016/j.jvolgeores.2012.01.001
732
733 Hubbard HH, Lansing D, Runyan H (1971) A review of Blade Noise Technology. J
734 Sound Vibration 19 (3), 227-249. doi: 10.1016/0022-460X(71)90686-9
735
736 Ichihara M, Ripepe M, Goto A, Oshima H, Aoyama H, Iguchi M, Tanaka K, Taniguchi
737 H (2009) Airwaves generated by an underwater explosion: Implications for volcanic
738 infrasound. J Geophys Res 114, B03210. doi:10.1029/2008JB005792
739
740 Iezzi AM, Fee D, Kim K, Jolly AD, Matoza RS, (2019) Three-Dimensional Acoustic
741 Multipole Waveform Inversion at Yasur Volcano. Vanuatu. J Geophys Res: Solid Earth
742 124.8, pp. 8679–8703. doi: 10.1029/2018jb017073
743

744 Jolly AD, Sherburn S, Jousset P, Kilgour G, (2010) Eruption source processes derived
745 from seismic and acoustic observations of the 25 September 2007 Ruapehu
746 eruption-North Island, New Zealand. J Volcanol Geotherm Res 191:33–45. doi:
747 10.1016/j.jvolgeores.2010.01.009
748
749 Jolly AD, Jousset P, Lyons JJ, Carniel R, Fournier N, Fry B, Miller C (2014)
750 Seismoacoustic evidence for an avalanche driven phreatic eruption through a beheaded
751 hydrothermal system: an example from the 2012 Tongariro eruption. J Volcanol and
752 Geotherm Res 286:331-347. doi: 10.1016/j.jvolgeores.2014.04.007
753
754 Jolly A, Kennedy B, Edwards M, Jousset P, Scheu B. (2016) Infrasound tremor from
755 bubble burst eruptions in the viscous shallow crater lake of White Island, New Zealand,
756 and its implications for interpreting volcanic source processes. J Volcanol Geotherm Res
757 327:585–603. doi: 10.1016/j.jvolgeores.2016.08.010
758
759 Jolly AD, Matoza RS, Fee D, Kennedy BM, Iezzi AM, Fitzgerald, RH, and others
760 (2017) Capturing the acoustic radiation pattern of Strombolian eruptions using
761 infrasound sensors aboard a tethered aerostat, Yasur volcano, Vanuatu. Geophys Res
762 Letts 44, 9672–9680. doi: 10.1002/2017GL074971
763
764 Jolly A, Lokmer I, Christenson B, Thun J (2018) Relating gas ascent to eruption
765 triggering for the April 27, 2016, White Island (Whakaari), New Zealand eruption
766 sequence. Earth Planets Space 70:177. doi: 10.1186/s40623-018-0948-8
767
768 Kanamori H, Given JW (1982) Analysis of long-period seismic waves excited by the
769 May 18, 1980, eruption of Mount St. Helens—A terrestrial monopole? J Geophys Res
770 82(B7):5422–5432. doi: 10.1029/JB087iB07p05422
771
772 Kieffer SW (1981) Blast dynamics at Mount St. Helens on 18 May 1980. Nature 291,
773 568–570. doi: 10.1038/291568a0
774
775 Kilgour G, Manville V, Della Pasqua F, Graettinger A, Hodgson KA, Jolly GE, (2010)
776 The 25 September 2007 eruption of Mount Ruapehu, New Zealand: directed ballistics,

surtseyan jets, and ice-slurry lahars. J Volcanol Geotherm Res 191:1–14. doi: 10.1016/j.jvolgeores.2009.10.015

Kilgour G, Kennedy B, Scott B, Christenson B, Jolly A, Asher C, Rosenberg M, Saunders K (2021) Whakaari/White Island: a review of New Zealand's most active volcano, New Zealand. J of Geol and Geophys 64:2-3: 273-295. doi: 10.1080/00288306.2021.1918186

Kim K, Lees JM, & Ruiz M (2012). Acoustic multipole source model for volcanic explosions and inversion for source parameters. Geophys J Int 191(3): 1192-1204. doi: 10.1111/j.1365-246X.2012.05696.x

Lighthill J (1978) Waves in fluids (2nd ed.). Press, Cambridge, U. K.: Cambridge University.

Lube G, Breard ECP, Cronin SJ, Proctor JN, Brenna M, Moebis A, and others (2014) Dynamics of surges generated by hydrothermal blasts during the 6 August 2012 Te Maari eruption, Mt. Tongariro, New Zealand. J Volc Geotherm Res 286: 348–366. doi: 10.1016/j.jvolgeores.2014.05.010

Lyons JJ, Haney MM, Fee D, Wech AG, Waythomas CF (2019) Infrasound from giant bubbles during explosive submarine eruptions. Nature Geosci 12(11): 952–958. doi: 10.1038/s41561-019-0461-0

Marcillo O, Johnson JB, Hart D (2012) Implementation, characterization, and evaluation of an inexpensive low-power low-noise infrasound sensor based on a micromachined differential pressure transducer and a mechanical filter. J Atmos Ocean Tech, 29. doi: 10.1175.JTECH-D-11-00101.1

Matoza RS, Garces MA, Chouet BA, D'Auria L, Hedlin MAH, De Groot-Hedlin C, & Waite, GP (2009) The source of infrasound associated with long-period events at Mount St. Helens. J Geophys Res: Solid Earth 114: B04305. doi: 10.1029/2008JB006128

Matoza RS, Fee D, Neilsen TB, Gee K., & Ogden DE (2013) Aeroacoustics of volcanic jets: Acoustic power estimation and jet velocity dependence. J Geophys Res: Solid Earth 118: 6269–6284. doi: 10.1002/2013JB010303

McNeal JS., Jones J, Cal RB, Mastin LG, Kim D, Solovitz SA (2018) Experimental study of analogue vent erosion towards nozzle shapes. J Volcanol Geotherm Res 367: 79-87. doi: 10.1016/j.jvolgeores.2018.10.022

Park I, Jolly A, Kim KY, Kennedy B (2019) Temporal variations of repeating low frequency volcanic earthquakes at Ngauruhoe Volcano, New Zealand. J Volcanol Geotherm Res 373:108–119. doi: 10.1016/j.jvolg eores.2019.01.024

Rowell CR, Fee D, Szuberla CA, Arnoult K, Matoza RS, Firstov PP, and others (2014) Three-dimensional volcano-acoustic source localization at Karymsky Volcano, Kamchatka, Russia. J of Volcanol and Geotherm Res 283: 101–115. doi: 10.1016/j.jvolgeores.2014.06.015

Sanderson RW, Matoza RS, Haymon RM, Steidl JH (2021) A Pilot Experiment on Infrasonic Lahar Detection at Mount Adams, Cascades: Ambient Infrasound and Wind‐Noise Characterization at a Quiescent Stratovolcano. Seis Res Lett 92 (5): 3065–3086. doi: 10.1785/0220200361

Sonder I, Graettinger A, Neilsen TB, Matoza RS, Taddeucci J, Oppenheimer J, Lev E Tsunematsu K, Waite G, Valentine GA , Befus KS (2022) Experimental multiblast craters and ejecta – seismo-acoustics, jet characteristics, craters, and ejecta deposits and implications for volcanic explosions. J Geophys Res Solid Earth 127, e2022JB023952, doi: 10.1029/2022JB023952.

Takarada S, Oikawa T, Furukawa R, and others (2016) Estimation of total discharged mass from the phreatic eruption of Ontake Volcano, central Japan, on September 27, 2014. Earth Planets and Space 68: 138. doi: 10.1186/s40623-016-0511-4

Tsunematsu K, Ishimine Y, Kaneko T. and others (2016) Estimation of ballistic block

843 landing energy during 2014 Mount Ontake eruption. Earth Planets and Space 68: 88
844 (2016). doi: 10.1186/s40623-016-0463-8
845
846 Watson LM, Dunham EM, Mohaddes D, Labahn J, Jaravel T, Ihme
847 M (2021) Infrasound radiation from impulsive volcanic eruptions: Nonlinear
848 aeroacoustic 2D simulations. J Geophys Res*:* Solid Earth 126: e2021JB021940. doi:
849 /10.1029/2021JB021940
850
851 Woulff G, McGetchin T (1976) Acoustic noise from volcanoes: Theory and experiment.
852 Geophysical Journal of the Royal Astronomical Society 45: 601–616. doi:
853 10.1111/j.1365-246X.1976.tb06913.x
854
855 Wadsworth FB, Unwin HE, and others (2018) Trashcano: Developing a quantitative
856 teaching tool to understand ballistics accelerated by explosive volcanic
857 eruptions. Volcanica 1(2): 107–126. doi: 10.30909/vol.01.02.107126
858
859 Zhang L, Wang H, Ruan W (2016) Experiments on Jet Noise Reduction with a Liquid
860 Column. Acoust Aust 44:291–297. doi: 10.1007/s40857-016-0056-5
861

862